Opto-electrical modelling and roadmap for 2T monolithic Perovskite/CIGS tandem solar cells

Procel, P.; Knobbe, J.; Rezaei, N.; Zardetto, V.; Phung, N.; Ma, M.; Santbergen, R.; Mazzarella, L.; Isabella, O.; More Authors

Opto-electrical modelling and roadmap for 2T monolithic Perovskite/CIGS tandem solar cells

P. Procel [a,*], J. Knobbe [a], N. Rezaei [a,b], V. Zardetto [c], N. Phung [d], M. Ma [e], M. Simor [c], M. Creatore [d], S. Veenstra [c], R. Santbergen [a], L. Mazzarella [a], O. Isabella [a]

[a] *PVMD group, Delft University of Technology, Delft, the Netherlands*
[b] *Inorganic Materials Science (IMS), University of Twente, Enschede, the Netherlands*
[c] *Department of Applied Physics, Eindhoven University of Technology, Eindhoven, the Netherlands*
[d] *TNO, partner in Solliance, High Tech Campus 21, Eindhoven, the Netherlands*
[e] *MiaSole Hi-Tech Corp, Supplier of CIGS Solar cells, 3211 Scott Blvd, Santa Clara, Ca, USA*

ABSTRACT

Two terminal (2T) perovskite/copper-indium-gallium-selenide (CIGS) tandem solar cells combine high conversion efficiency with lightweight flexible substrates which can decrease manufacturing and installation costs. In order to improve the power conversion efficiency of these tandem solar cells, the use of advanced simulation tools is crucial to estimate the loss mechanisms. In this regard, most of the available simulation works on tandem solar cells are oriented to minimize optical losses and assuming simplifications for the electrical simulations in particular in the top and bottom cell interconnection at the so-called tunnel recombination junction (TRJ) neglecting the inner physics of the complete tandem device. Therefore, the effect of charge exchange mechanism between top and bottom soler cells on the external parameters of a tandem devices is not fully understood yet. In this work, we present an experimentally validated opto-electrical model based on the fundamental semiconductor equations for the study of loss mechanisms of a reference perovskite/CIGS solar cell. Different from other numerical works, because our simulation platform includes the fundamental working mechanisms of the layers comprising the TRJ, we can properly calculate the losses related to it. We firstly present the calibration and validation of our opto-electrical model with respect to three fabricated reference solar cells: top cell only, bottom cell only and tandem device. Then, we use the calibrated model to evaluate main loss mechanisms affecting the baseline tandem device. Finally, we use the model to propose a roadmap for the optimization of monolithic perovskite/CIGS tandem solar cells.

1. Introduction

Multi-junction architectures allow overcoming the limitation of power conversion efficiency (η) of single junction solar cells. For that reason, the photovoltaic (PV) community focuses recently on tandem hybrid architectures, combining a wide bandgap top cell based on a metal halide perovskite absorber with a commercial lower bandgap bottom PV device such as crystalline silicon (c-Si) or copper indium gallium selenide (CIGS). The advantage of the tandem perovskite/CIGS architecture, over the c-Si counterpart, lays in its compatibility with lightweight flexible substrates by means of roll to roll (R2R) manufacturing, which can further reduce the manufacturing and the installation costs. Additionally, such a flexible tandem structure will promote the application of PV devices in building (BIPV), vehicle (VIPV), and construction elements. In this context, research and development groups have previously investigated tandem solar cells based on perovskite/CIGS [1–4].

Although the PV market is primarily dominated by silicon-based wafers, CIGS thin-film technology has the potential to achieve an even lower environmental footprint by using less material with low-cost processes in their production [5]. In addition, the bandgap of the CIGS bottom sub-cell can be adjusted down to 1 eV to suit better the combination with the 1.5–1.7 eV bandgap range of perovskite top sub-cell, thus increasing the amount of light absorbed in both sub-cells [6]. The highest reported efficiency for perovskite/CIGS monolithic two terminal (2T) tandem solar cells is 24.2 % (certified) [7]. In order to achieve the potential efficiency over 30 % [2], specialized analysis of loss mechanisms is crucial for these tandem solar cells. With the aim of proposing guidelines to experimentally reach such theoretical performance, opto-electrical simulations are a great asset, supporting in the process the design of such thin-film tandem solar cells. Most of the available simulation works on tandem solar cells are oriented to minimize optical losses [7–14]. Commonly, opto-electrical simulations of 2T tandem solar cells assume simplifications in the models specially with respect to the interconnection of the two sub-cells [15,16], thus neglecting the inner physics of the so-called tunnel recombination junction (TRJ). In turn,

---

* Corresponding author.
E-mail address: p.a.procelmoya@tudelft.nl (P. Procel).

these simplifications make the assessment of opto-electrical losses of tandem solar cells a challenging task. Thus, the impact of charge transport mechanisms occurring in TRJ on the external parameters of a tandem devices is not well understood yet.

In this work, we present an experimentally validated opto-electrical model based on the fundamental semiconductor equations for the study of loss mechanisms of a reference perovskite/CIGS solar cell. Different from other numerical works, because our simulation platform includes the fundamental working mechanisms of the layers comprising the TRJ, we can properly calculate the losses related to it. We firstly present the calibration and validation of our opto-electrical model with respect to three fabricated reference solar cells: top cell only, bottom cell only and tandem device. Then, we use the calibrated model to evaluate main loss mechanisms affecting the baseline tandem device. Finally, we use the model to propose a roadmap for the optimization of monolithic perovskite/CIGS tandem solar cells.

2. Experimental and modelling methodology

CIGS devices were received from *MiaSole* company. For their use in 2T tandem solar cells, they were chemically etched to remove the ZnO-based top layers. After that, new intrinsic ZnO was sputtered and the TRJ was formed between spatial atomic layer deposited (ALD) SnO_2 and PEDOT:PSS as described in a previous work (no gold used here) [17]. Then the top cell is built as follows: poly (triarylamine) (PTAA) in Toluene (2 mg/mL) is spin-coated at 5000 rpm for 35 s followed by annealing at 100 °C for 10 min. Dual-cation perovskite $Cs_{0.15}FA_{0.85}Pb$ $(I_{0.92}Br_{0.08})_3$ perovskite solution is prepared by mixing a stoichiometric amount of the following precursors: PbI_2 (Alfa Aesar, 99.999 %) and $PbBr_2$ (Tokyo Chemical Industry, 99.9 %), FAI (Greatcell (Dyesol), 99.9 %), and CsI (Alfa Aesar, 99.9 %), in anhydrous DMF:DMSO (Sigma-Aldrich, >99.9 %) (9:1 vol ratio), to achieve a concentration of 1.33 M. Such solution is spin-coated with a two-step procedure: at 2000 rpm for 10 s and 5000 rpm for 30 s. 250 µL of chlorobenzene is dropped on the spinning substrate 21 s after the start of the program to quench the film and form a smooth and compact layer. The film is subsequently annealed on a hotplate at 100 °C for 10 min. For the electron transport layer (ETL), a 20 mg/mL PCBM (Solenne B·V., 99 %) solution in chlorobenzene is spin-coated onto the perovskite layer at 1500 rpm for 50 s, followed by 45-nm thick SnO_2 deposited by spatial ALD. Finally, 80-nm thick ITO is sputtered, followed by 100-nm thick silver grids. The fabrication sequence of the perovskite-based single junction solar cell is essentially similar with only two notable differences: (1) the PTAA is spin coated on ITO-coated soda lime glass (SLG) and (2) 160-nm thick MgF_2 is deposited on the outer side of said SLG substrate (see Fig. 1a). Current density-voltage (*J-V*) measurements were carried out using WACOM dual source solar simulator which is calibrated with a Si reference cell to emulate the AM1.5G spectrum. The cell area of 0.25 cm^2 is defined by a shadow mask. The scan speed is 200 mV/s with a step size of 20 mV controlled by a Keithley 2400 source-measure unit. The maximum power point tracking (MPPT) is performed for 3 min. EQE measurements were recorded with a home-built setup using chopped monochromatic light from a Xenon lamp. EQE is measured for each sub-cell. NIR light (LED emission at 850 nm) was used to saturate the CIGS cell and record the EQE of the top perovskite cell. Blue light (LED emission at 455 nm) was used instead to saturate the top perovskite cell and get the contribution of the bottom CIGS cell. No electrical bias was required.

For the opto-electrical modelling, we implement a two-dimensional model of 2T perovskite/CIGS tandem solar cell in TCAD Sentaurus [18], coupled with optical simulator GenPro4 [19]. Accordingly, our optical modelling considers wave and ray optics to obtain an optical generation profile localized in the absorber materials. Our simulation framework solves the semiconductor equations assuming that the solar cells are based on inorganic materials, including transport at hetero-interfaces by means of tunneling and thermionic emission models
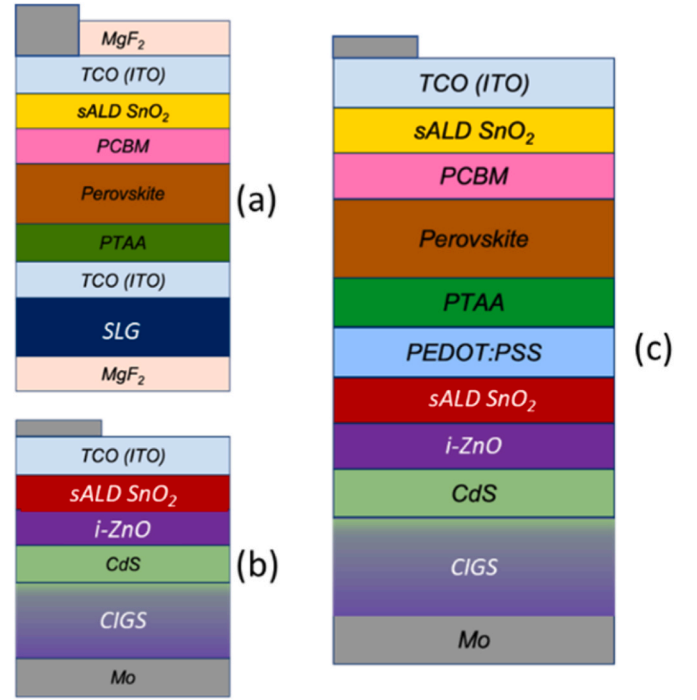
consistently coupled to the drift-diffusion model [18].

The model parameters for the simulation of the perovskite top cell (Fig. 1a) and the CIGS bottom cell (Fig. 1b) are summarized in Table 1 and Table 2, respectively. To model the bandgap grading in CIGS, we use an energy-shift model to estimate bandgap and optical parameters according to the gallium (Ga) profile in CIGS material [20]. We replicate the transient performance of the solar cells, accounting for the equivalent recombination mechanisms. To this aim, we included energy states distributions with parameters reported in Table 3. Additionally, we account for a spatial distribution of defect states in the perovskite material as reported in Ref. [21], which is tailored in two exponential distributions [22] (see parameters reported in Table 4). Similarly, we consider the intrinsic recombination model for perovskite reported in Ref. [22]. To simulate the tandem solar cell, we include PEDOT:PSS and SnO_2 layers as TRJ to couple the top and bottom solar cells. Note that we use non-local tunneling models including band-to-band tunneling (B2BT) and trap assisted tunneling (TAT) as fundamental transport mechanisms

Fig. 1. Schematic structure of the reference (a) perovskite single junction, (b) CIGS single junction and (c) perovskite/CIGS tandem solar cell (dimensions are not in scale).

Table 1
Model parameters of top cell.

Material parameters	ITO [23, 24]	SnO_2 [25]	PCBM [26]	Perovskite [25,27,28]	PTAA [29,30]
Thickness (nm)	180	45	40	450	10
Bandgap (eV)	3.7	4.25	1.6	1.6	3.3
Electron affinity (eV)	4.9	3.71	4.3	3.9	1.8
Permittivity	3.5	10	3	6.5	3
Doping (cm^{-3})	2×10^{20},n	3×10^{18}, n	7×10^{17}, n	1×10^{16}, n	1×10^{18}, p
CB DOS (cm^{-3})	4.1×10^{18}	4×10^{18}	2.2×10^{19}	1×10^{20}	2.2×10^{18}
VB DOS (cm^{-3})	1.7×10^{19}	1×10^{18}	1.8×10^{18}	1×10^{19}	1.8×10^{19}
Mobility e, h ($cm^2V^{-1}s^{-1}$)	45, 40	1×10^{-3}, 0.25	4×10^{-4}, 4×10^{-4}	35, 35	4×10^{-5}, 4×10^{-5}

Table 2
Model parameters of bottom cell.

Material parameters	i-ZnO [31]	CdS [31–33]	CIGS [31,34]
Thickness (nm)	45	40	2500
Bandgap (eV)	3.3	2.4	Graded [20]
Electron affinity (eV)	4.3	4.2	Graded [20]
Permittivity	9	10	13.6
Doping (cm^{-3})	1×10^{17}, n	8×10^{16}, n	2×10^{16}, p
CB DOS (cm^{-3})	3×10^{18}	1.3×10^{18}	6.8×10^{17}
VB DOS (cm^{-3})	1.7×10^{19}	1×10^{19}	1.5×10^{19}
Mobility e, h (cm^{2}V^{-1}s^{-1})	100, 30	72, 20	100, 12.5

associated with semiconductor materials [23]. Table 5 summarizes model parameters of the TRJ region.

3. Calibration of the opto-electrical model

We calibrate our model by comparing *J-V* curves of simulated devices with those of baseline experimental devices. Due to the inherent complexity of the tandem solar cell, we firstly calibrate our simulation model with stand-alone top and bottom cells in single junction configuration using the same stack of layers (see Fig. 1) measured under standard test conditions. At this stage, due to the non-optimized perovskite top subcell, which absorbs vast part of the incoming light, the bottom subcell limits the tandem resulting in a heavily current-mismatched tandem device. Note that the top and bottom sub-cells of the tandem are very similar to the individual single junction perovskite and CIGS reference cells, as the materials and fabrication processes correspond to the same batch of experiments. Afterwards, we use the calibrated model and parameters in the tandem device including the TRJ layers [17] and tune the B2BT and TAT charge transport models. In this regard, we calibrate the energy alignment at TRJ with parameters in Table 5 consistent with values reported in Refs. [25,37] assuming carrier concentration as active doping at SnO$_2$ and PEDOT:PSS. Fig. 2 shows the comparison between the experimental and simulated data of single junction perovskite, single junction CIGS, and perovskite/CIGS tandem solar cell under illumination (Fig. 2a). Fig. 2b shows J-V response of tandem baseline in dark conditions using the same input parameters as in illumination conditions. This further confirms that our model replicates the inner physics of the baseline tandem solar cell. A reasonable match between simulated and measured external parameters of the three solar cells indicates that our model replicates well the inner physics of the tandem solar cell (Table 6). The calibration of perovskite solar cell is achieved by adjusting the parameters of the spatial-dependent defect distribution in perovskite material. The calibration of CIGS solar cell is reached by tuning the CIGS thickness and spatial bandgap as reported in Ref. [20]. Thus, in our simulations which features a flat CIGS/CdS interface, we account for the CIGS roughness from SEM images of fabricated CIGS solar cell [40,41]. For the tandem solar cell fitting, we tune the TAT model by incorporating a defect distribution in PEDOT:PSS material. The resulting material parameters of the calibration are reported in Table 3.

4. Opto-electrical losses in baseline 2T tandem solar cell

Using our calibrated simulation platform, we studied the opto-electrical losses occurring inside the baseline tandem solar cell. From the optical point of view, Fig. 3a shows the absorbed photocurrent (J_{ph}) in top cell, bottom cell, optical parasitic absorption in supporting layers and reflectance losses. Each spectral contribution is integrated with the AM1.5 photon flux between 300 and 1200 nm to express a single value in terms of photocurrent density. Note that CIGS absorbs light spectra up to 1200 nm. The sum of absorbed light and losses results in a maximum photocurrent of 46.68 mA/cm^2 (J_{ph}) in the studied wavelength range. We observe that the total implied photocurrent in perovskite and CIGS absorber layers is 16.67 (J_{top}) and 13.54 mA/cm^2 (J_{bottom}), respectively, with a total absorbed 30.21 mA/cm^2 photocurrent density. This reveals that the implied photocurrent density is limited by the bottom cell to 13.54 mA/cm^2 due to the current mismatch between top and bottom sub-cells. We notice that the reflectance losses are still substantial contributing to an optical loss of 10.96 mA/cm^2 including 3.25 mA/cm^2 of front contact shading losses. The optical losses due to reflectance are ascribed to three different components. Following the method described in Ref. [8], we estimated 2.53 mA/cm^2 implied photocurrent density lost as reflectance occurring at front side of the tandem, 3.01 mA/cm^2 lost as intermediate reflectance at TRJ interlayers, and 2.12 mA/cm^2 lost as rear reflectance at bottom side of the tandem solar cell. Regarding parasitic absorption losses with 5.52 mA/cm^2, we observe that the main contribution comes from molybdenum (Mo), front TCO, PCBM and PEDOT:PSS with 2.1, 1.2, 0.9 and 0.8 mA/cm^2, respectively. Fig. 3b and c reports the breakdown of recombination mechanisms using the absorbed photocurrent in top (J_{top}) and bottom (J_{bottom}) cells,

Table 4
Parameters of spatial distribution of energy states in perovskite material used for calibration of our model.

Region	Defect density (cm^{-3}eV^{-1})
Perovskite/PTAA	1×10^{17}
Perovskite/PCBM	1×10^{15}
Perovskite bulk	1×10^{14}

Table 5
Model parameters of the tunnel recombination junction (TRJ).

Material parameters	PEDOT:PSS [35–37]	s-SnO$_2$ [25]	NiO$_x$ [38,39]
Thickness (nm)	40	15	40
Bandgap (eV)	1.6	3.6	3.84
Electron affinity (eV)	3.6	4.0	1.4
Permittivity	3	10	11.9
Carrier concentration (cm^{-3})	1.1×10^{18}	5×10^{19}	4.63×10^{19}
CB DOS (cm^{-3})	2.2×10^{18}	4×10^{18}	2.2×10^{18}
VB DOS (cm^{-3})	1.8×10^{19}	1×10^{18}	1.8×10^{19}
Mobility e, h (cm^{2}V^{-1}s^{-1})	100, 100	15, 15	1×10^{-3}, 1×10^{-3}
Defect density (cm^{-3}eV^{-1})	1×10^{18}	–	–
Energy level defect	Mid-gap	–	–
Capture cross section e, h (cm^{2}s^{-1})	5×10^{-15}, 1×10^{-15}	–	–
Standard deviation of defect dist. (Gaussian) (eV)	0.5	–	–
Effective tunneling mass	0.1 m$_0$	0.1 m$_0$	0.1 m$_0$

*m$_0$ is the electron rest mass.

Table 3
Parameters of energy states distributions used for calibration of our model.

| Material parameters	CIGS [31]		CdS	CIGS/CdS	i-ZnO	Perovskite
Defect density (cm^{-3}eV^{-1})	5×10^{13}	1×10^{12}	5×10^{15}	1×10^{12}	1×10^{16}	See Table 4
Energy level	Mid-gap	0.2 eV (VB)	Mid-gap	Mid-gap	Mid-gap	Mid-gap
Capture cross section e, h (cm^{2}s^{-1})	5×10^{-13}, 1×10^{-15}	5×10^{-13}, 1×10^{-15}	5×10^{-13}, 1×10^{-15}	5×10^{-13}, 1×10^{-15}	5×10^{-13}, 1×10^{-15}	1×10^{-17}, 1×10^{-17}
Type	Donor	Acceptor	Acceptor	Acceptor	Acceptor	Donor
Standard deviation (Gaussian) (eV)	0.5	0.5	0.5	0.5	0.5	–
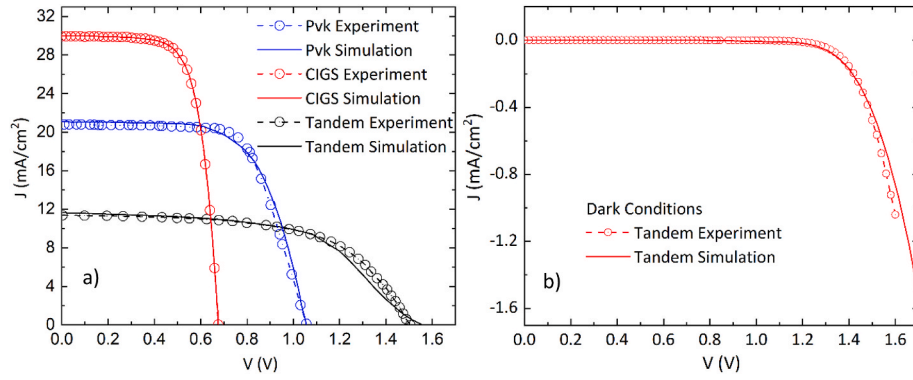
Fig. 2. J-V curves of the simulated and experimental a) perovskite (Pvk), CIGS and tandem solar cells under illumination. b) tandem solar cell in dark conditions. The same set of input parameters was used for simulating both illuminated and dark conditions.

Table 6
Measured and simulated external parameters of the baseline perovskite, CIGS, and tandem solar cells.

External parameters	J_{sc} (mA/cm^2)	V_{oc} (V)	FF (%)	η (%)
Perovskite exp.	20.11	1.051	64.33	14.34
Perovskite sim.	20.83	1.052	66.08	14.45
CIGS exp.	31.8	0.688	72.05	15.76
CIGS sim.	31.82	0.692	72.09	15.89
Tandem exp.	11.38	1.509	59.33	10.19
Tandem sim.	11.94	1.567	56.9	10.63

respectively, as reference. For the top and bottom cells, we calculate a J_{sc} of 11.94 mA/cm^2, which as expected is identical for top and bottom cell as both cells are connected in series. We note that recombination due to defects in the top cell is: 3.889 and 0.823 mA/cm^2 for the bulk and its interfaces, respectively. In the case of the bottom cell, we calculated 1.053 and 0.54 mA/cm^2 for recombination in the bulk and its interfaces, respectively. We notice that radiative recombination contribution is minimal as 0.002 mA/cm^2. It is worth noting that Shockley-Read-Hall (SRH) recombination difference between top (4.7 mA/cm^2) and bottom cell (1.6 mA/cm^2) is 3.1 mA/cm^2, which is similar to the 3.13 mA/cm^2 difference between absorbed photocurrent in top (16.6 mA/cm^2) and bottom cell (13.54 mA/cm^2). This indicates that SRH recombination mechanisms in the top cell compensate the mismatch in absorbed photocurrent in top and bottom structures to achieve the 11.94 mA/cm^2 J_{sc} of the tandem device following the charge conservation principle within the tandem solar cell.

5. Analysis of the tunnel recombination junction

In our simulation framework, we model the TRJ structure based on fundamental semiconductor equations, and we study its charge transfer mechanisms in our baseline tandem solar cell. Charge transport in the TRJ is established by B2BT and TAT mechanisms, depending on the energy band alignment [23] of the two complementary layers: PEDOT: PSS and SnO$_2$. Fig. 4 illustrates two schematic band diagrams of the TRJ for two different cases: with and without energy band alignment. In principle, the energy alignment is defined by the energy of the conduction or valence band (E_V) with respect to the Fermi energy in both layers. Thus, carrier population in both layers is dominated by electrons in SnO$_2$ and holes in PEDOT:PSS. Accordingly, electrons (holes) in SnO$_2$ (PEDOT:PSS) are accumulated where the energy of the conduction (valence) band is close to Fermi energy. The recombination between holes from PEDOT:PSS and electrons from SnO$_2$ happens depending on the spatial and energetic components of the accumulation regions [42]. Optimal recombination based on B2BT mechanisms occurs when the accumulation regions in SnO$_2$ and PEDOT:PSS are energetically aligned as Fig. 4a shows. In the absence of such alignment, charge exchange is based on intermediate energy states as TAT mechanisms, depicted inFig. 4b. TRJ layers in our baseline device, are not energetically aligned, thus charge exchange occurs via TAT. Note that a validation of our model is only possible implementing TAT tunneling as explained in Section 3.

To evaluate the transport in TRJ, we simulate our baseline tandem solar cell considering different energy alignment in terms of the energy gap between the Fermi level (conduction band) and the valence band (Fermi level) in PEDOT:PSS (SnO$_2$) of the TRJ. Note that we quantify the energy alignment effect in terms of ΔE: E_c-E_f for SnO$_2$ and E_f-E_v for PEDOT:PSS. To do so, we adjusted carrier concentration in both layers as we associate active doping in our model to the carrier concentration. Our simulations cover different devices with energy alignment in the range of −75 to 75 meV for SnO$_2$ and 0–125 meV for PEDOT:PSS. Fig. 5 reports the simulated external parameters of our reference device as a function of the energy alignment at the SnO$_2$/PEDOT:PSS interface. In general, we observe higher external parameter values for SnO$_2$ E_c-E_f
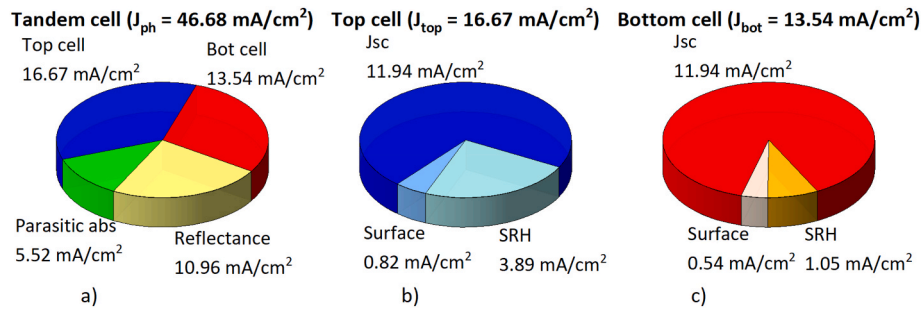

Fig. 3. Breakdown of (a) the incident photocurrent density in the tandem solar cell, (b) the absorbed photocurrent in top cell and (c) the absorbed photocurrent in bottom cell. J_{ph} is the AM1.5 photocurrent between 300 and 1200 nm, J_{top} is the photocurrent generated in top perovskite solar cell and J_{bottom} is the photocurrent generated in bottom CIGS solar cell. SRH and Surf stand for Shockley-Read-Hall recombination in bulk and recombination at interfaces, respectively.
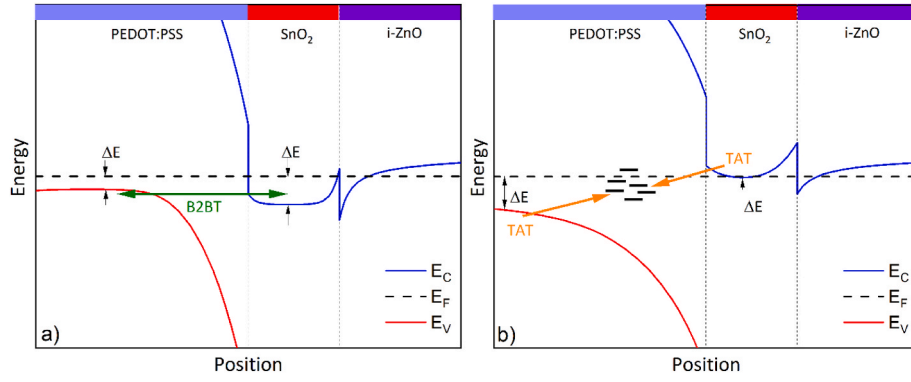
Fig. 4. Energy band diagram of PEDOT:PSS/SnO$_2$ TRJ illustrating the case of (a) B2BT or (b) TAT mechanisms. Note the energy (mis-)alignment of the E$_v$ in PEDOT:PSS with the E$_c$ in SnO$_2$ as the triggering condition for B2BT or TAT. E$_v$ and E$_c$ stand for valence and conduction bands. ΔE stands for E$_c$-E$_f$ and E$_f$-E$_v$ for SnO$_2$ or PEDOT:PSS, respectively.

ranging from −75 to 0 meV together with PEDOT:PSS E$_f$-E$_v$ from 20 to 72 meV. Such energy alignment allows B2BT with direct energy transitions, which is more efficient than the TAT counterpart [23]. Interestingly, we observe the same trends among all the parameters: J_{sc}, V_{oc}, FF and η. This fact is particularly relevant, because it reveals the importance of an optimal TRJ in tandem solar cells. The energy alignment in TRJ layers potentially affects all the external parameters of the tandem device. In fact, within our simulation domain, J_{sc}, V_{oc}, FF and η variation is 8 %, 50 %, 34 % and 24 %, respectively (see Fig. 5a, b, 5c and 5d). As expected, higher parameter values (red tones in Fig. 5) are obtained for devices with energy alignment that allows B2BT mechanisms for charge exchange. In Fig. 5, the effect of the transition of the transport dominated by TAT to B2BT mechanisms is observed for low values of E$_f$-E$_v$ in PEDOT:PSS (12.5 meV $< \Delta Ep <$ 65 meV). This corresponds to a p-type material with the Fermi level close to the valence band energy.

For the n-type material in the TRJ, a higher carrier concentration results in a negative value for Ec-Ef which is preferred for the TRJ structure. This means that the Fermi energy surpasses the conduction band energy (E$_C$) as an inherent property of highly conductive materials acting as degenerate semiconductors. Interestingly, SnO$_2$ already exhibits such favourable conditions in our baseline device (see Table 5 and Fig. 5). However, PEDOT:PSS properties are insufficient to achieve the optimal alignment in the TRJ structure. Indeed, we calculate that achieving the proper energy alignment in TRJ layers potentially improves the η by around 2%$_{abs}$.

6. Road to improvement

After assessing the opto-electrical loss mechanisms, we deployed our simulation framework to draw a roadmap for performance improvement
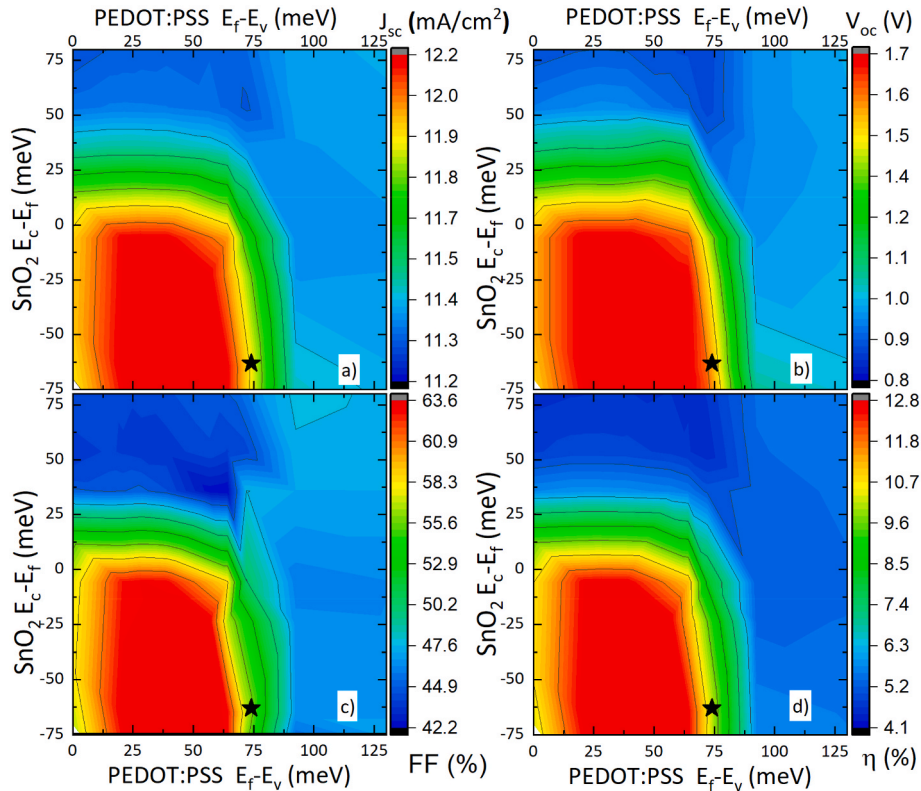

Fig. 5. Contour plot of the simulated external parameters of the 2T tandem solar cells: (a) J_{sc}, (b) V_{oc}, (c) FF and (d) η as a function of energy alignment in SnO$_2$ (E$_c$-E$_f$)) and PEDOT:PSS (E$_f$-E$_v$). Note that star symbol indicates the energy alignment of the baseline tandem device.

of the tandem solar cell considering the realization of our tandem solar cell based on a commercially available CIGS solar cell. To account for such a condition, all parameters from CIGS bottom cell have been kept constant. Therefore, we present the following path: (i) TRJ optimization, (ii) optical enhancement, (iii) transport in top sub-cell and (iv) passivation in top sub-cell. In each step, we focus on a group of parameters that significantly affect each mechansim to optimize. After each step, the optimal parameter value is selected for the subsequent simulations to provide the optimization path of the tandem solar cell.

6.1. TRJ optimization

In the previous section, we mentioned the relevance of TRJ layers in the performance of the tandem device. We also pointed out that the main limitations in TRJ are due to the PEDOT:PSS layer. Therefore, we propose the use of a different material to accomplish the energy alignment condition. In this respect, NiO_x has been reported as a promising candidate for hole transport in TRJ structures [2,38,43,44]. In-house measurements resulted in bandgap, electron affinity and carrier concentration values of 3.82 eV, 1.36 eV and 4.63×10^{19} cm^{-3} as summarized in Table 5. In general the material exhibits interesting features, including a relatively high work function of 5 eV. Moreover, the relatively low electron affinity compared to SnO_2 leads to a conduction band offset of 2.6 eV wich is higher than that of PEDOT:PSS (0.4 eV). Note that the conduction band offset is defined by the difference between electron affinity of two adjacent materials. A high conduction band offset builds a high energy barrier for electrons towards the conduction band. Accordingly electrons tend to tunnel to the valence band energy of NiO_x which supports the transport of charge in TRJ structure. For the sake of simplicity, we assume the same thickness for NiO_x as PEDOT:PSS in our baseline solar cell. Fig. 6a and b show the energy band diagram of our baseline tandem solar cell using PEDOT:PSS and NiO_x respectively. In the baseline solar cell, we observe an energy band mis-alignment between valence and conduction band at PEDOT:PSS and SnO_2, respectively, as Fig. 6a illustrates. We observe a promising energy band alignment when replacing PEDOT:PSS by NiO_x in Fig. 6b. Indeed NiO_x enables efficient B2BT mechanisms with a calculated η of 12.91 %. Note that according to Fig. 6b, the energy alignment in NiO_x is achieved at 15 nm from the interface with SnO_2, indicating that NiO_x thickness could be decreased up to 15 nm, besides optical considerations changes in the intermediate reflectance [8].

6.2. Optical enhancement

In Section 4, we noted a 3.13 mA/cm^2 difference in absorbed photocurrent in both absorbers (see Fig. 3a) and an implied photocurrent density loss of 10.96 mA/cm^2 due to reflection. Accordingly, we propose a strategy to reduce such optical losses by improving the light management. We adjust the thickness of perovskite absorber to achieve

absorbed photocurrent matching in the two sub-cells. We found an optimal thickness value of 312 nm for the perovskite layer with a reduction of 138 nm from the reference thickness. With a thinner perovskite absorber, we reduced the absorbed photocurrent in the top cell, and in turn we increase the absorbed photocurrent in CIGS bottm cell to 14.95 mA/cm^2 which is 1.41 mA/cm^2 higher than the initial recorded value. To reduce reflectance losses, we applied an additional anti-reflective coating (ARC) at the front side of the tandem solar cell. Thus, we simulated the reference device with the addition of 100-nm thick MgF_2 top layer. MgF_2 is a traditional dielectric material used for improving the light management in lab-scale solar cells [45] and it is recommended for minimizing optical losses in tandem solar cells [8]. For our simulations, we use MgF_2 refractive indexes reported in Ref. [19]. We calculated that the absorbed photocurrent in both absorbers increases up to 16.68 mA/cm^2. Finally, to reduce shadowing losses, we evaluated the reduction of front metallization from 35 μm (7 % of front area) to 5 μm (1 % of front area) resulting in 17.17 mA/cm^2 absorber photocurrent in both absorbers. We simulated an overall η of 24.37 % for the optimized tandem solar cell after implementing the abovementioned optical enhancements. It is worth noting that at this stage, calculated η is higher than the current 24.2 % world record [7]. It has to be noted that achieving optical balance between top and bottom solar cells reduces recombination mechanisms that compensate the current balance as mentioned in Section 5. Thus, the tandem solar cell exhibits a 0.14 V increase in V_{oc} due to the reduction of recombination in the top solar cell.

6.3. Transport in top sub-cell

At the electron transport layer (ETL) side of the top cell, we observed an energy barrier in the conduction band that is opposing to the collection of electrons as Fig. 7a illustrates. Such energy barrier is formed by the conduction band offset of SnO_2 with PCBM (0.59 eV) and ITO (1.19 eV). In our reference solar cell we are using a SnO_2 layer deposited at 50 °C. It is known that electronic parameters of SnO_2 change depending on the crystallinity associated to processing conditions such as deposition temperature [25] and method [46]. To evaluate the energy barrier resulting from a more crystalline SnO_2, we update the parameters of SnO_2 using values measured on a film deposited at higher temperature of 200 °C [25]. Therefore, we accounted for electron affinity, bandgap, carrier concentration and mobility of 4.32 eV, 3.25 eV, 9.6×10^{19} cm^{-3} and 36 cm^{2}V^{-1}s^{-1}, respectively (see Fig. 7b). We noted a clear decrease in the energy barrier in the conduction band for the case of 200 °C SnO_2. Such an effect improves the FF of the tandem device from 79.05 % to 81.41 % and, consequently, an efficiency gain from 24.37 % to 25.13 %. Note that for facilitating the transport of electrons, an ETL material has to generally exhibit low work function and form a lower energy barrier at the heterointerface in terms of low conduction energy band offset, as in the case of SnO_2 deposited at 200 °C.
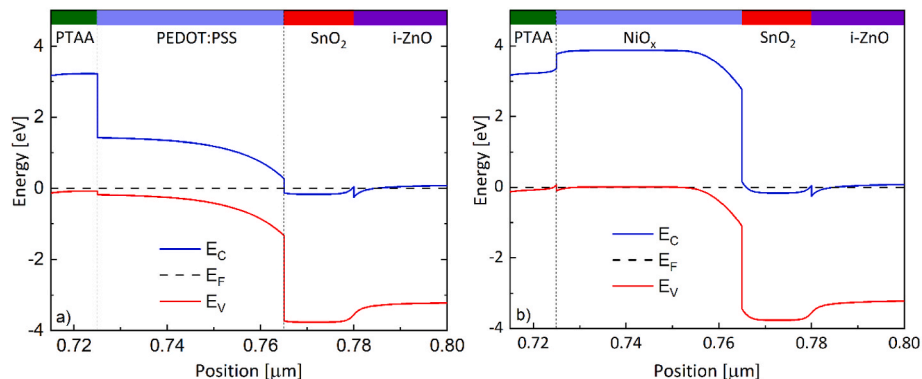

Fig. 6. Energy band diagram of the TRJ of the (a) baseline solar cell using PEDOT:PSS and SnO_2 and (b) using NiOx and SnO_2.
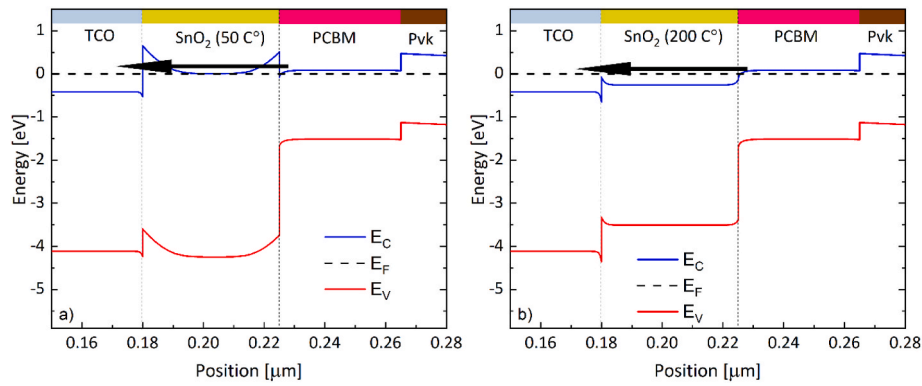
Fig. 7. *Energy band diagram indicating the ETL energy barriers alignment in the SnO$_2$ (yellow) and PCBM (pink) in the top cell using parameters of SnO$_2$ from different processes* [25]: *(a) SnO$_2$ at 50 °C and (b) SnO$_2$ (200 °C). Black arrow illustrates the direction of collecting electrons.*

Despite the theoretical electronic benefits of SnO$_2$ processed at 200 °C, it has to be noted that due to processing constrains of perovskite top cell, the processing of such SnO$_2$ could be detrimental for the perovskite material. Although such processing temperature is not compatible with the current perovskite stack, the layer parameters can give an indication for the electrical optimization of the low temperature SnO$_2$ ALD process [46].

6.4. Passivation in top sub-cell

So far, the passivation and bulk quality of the perovskite absorber is fixed in terms of defects parameters as reported in Table 4. Considering that the quality of the material and interfaces with ETL and HTL can be furhter improved [47–49], we investigate the impact of decreasing the defect density of these interfacnes on the external parameters of the tandem solar cell. In particular, pasivation of perovskite solar cells is achieved controlling the amount of PbI$_2$, using (i) additives such as elemental iodine, organic surfactants, and Group 1 metal compounds, as well as (ii) 2D perovskites or hydrophobic large cation molecules forming 2D or quasi-2D phases at grain boundaries or film surfaces providing passivation [50]. As expected, we observe 0.1 V increase in V_{oc} by reducing the defect density in perovskite material. In particular, the improvement becomes apparent by reducing the defect density at the perovskite/PTAA interface. At this point, as discussed in Section 6.3, the impact of bulk and perovskite/PCBM interface recombination is minimal and ascribed to the improved transport at PCBM/SnO$_2$ interface, which, avoiding the carriers accumulation, therefore minimizes the recombination. We calculated an increase in V_{oc} and FF from 1.57 to 1.66 V and 81.4–83.87 %, respectively, with a resulting in efficiencyof 26.69 %.

Overall, our simulation results show the potential improvements resulting from the adoption of four main changes in the device structure and suggesting a roadmap to achieve record perovskite/CIGS tandem solar cells. Table 7 and Fig. 8 indicate the calculated external parameters and the simulated *J-V* curves based on the disucssed improvement steps. It is worth mentioning that we have based our calculations on the same commercially available CIGS. Under these assumptions, we estimate 26.69 % conversion efficiency after short-term improvement for our tandem structure. It is worth noting that for such a limit we considered the existing CIGS and perovskite quality. However, further enhancement can be achieved by adjusting the bandgap of the bottom cell [7], applying passivation in the bottom CIGS contact at CIGS/Mo interface [41,51–53] and improving perovskite/CIGS quality.

7. Conclusions

In this work, we have presented an opto-electrical modelling, that enables to assess the opto-electrical losses and optimize a baseline

Table 7
Summary of external parameters calculated in the roadmap for performance improvement of the tandem solar cell.

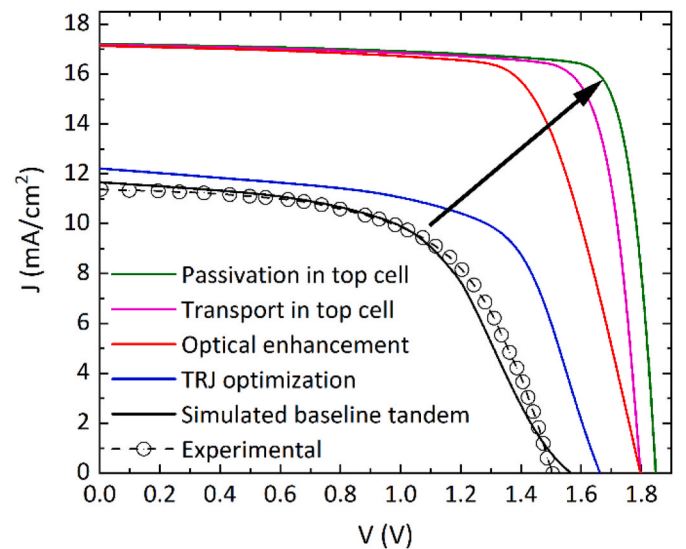| Initial tandem device	Improvement steps	Jsc (mA/cm^2)	Voc (V)	FF (%)	η (%)
Baseline (exp.)		11.38	1.51	59.33	10.19
Baseline (sim.)		11.94	1.57	56.90	10.63
	1. TRJ optimization	12.21	1.66	63.60	12.91
	2.Optical enhancement	17.16	1.80	79.05	24.37
	3. Transport in top cell	17.17	1.80	81.45	25.13
	4. Passivation in top cell	17.20	1.85	83.87	26.69

Fig. 8. Simulated J-V curves of the proposed roadmap using as reference the experimental tandem solar cell.

perovskite/CIGS tandem solar cell. The investigation has been carried out coupling GenPro4 and TCAD platforms for optical and electrical simulation, respectively, of the tandem solar cell. Our model was based on a novel approach that includes the accurate and self-consistent electrical modelling of the TRJ. We initially developed and calibrated the simulation framework with respect to electrical parameters of three different experimentally fabricated solar cell devices: single junction perovskite solar cell, single junction CIGS solar cell and tandem perovskite/CIGS solar cell with similar stack of materials.

As a result of the calibration process, we calculated and identified the main loss mechanisms of our baseline tandem solar cell. From the optical perspective, reflectance, and parasitic absorption mechanisms make up 10.92 and 5.32 mA/cm^2 photocurrent density losses. Additionally, the loss assessment shows that an unbalanced generation of carriers in top and bottom cells results in an implied photocurrent of 13.54 mA/cm^2 due to the limiting bottom cell. In short-circuit conditions, SRH recombination losses in the top and bottom sub-cells account for 4.71 mA/cm^2 and 1.59 mA/cm^2, respectively. Considering that the bottom cell limits the photo-generated current, SRH recombination in the top cell is dominant because it works as compensation mechanism to achieve the same J_{sc} in both sub cells. We show that the energy alignment in TRJ layers strongly impacts the external parameters of the baseline tandem solar cell. In particular, for the baseline tandem solar cell, our simulations reveal that the energy alignment between the TRJ layers leads to inefficient TAT mechanisms mostly due to PEDOT:PSS electronic properties. We demonstrate that B2BT mechanisms are preferred for charge exchange in TRJ to enable improved solar cell external parameters. Furthermore, our simulations show V_{oc} and FF gain up to 50 and 34 %, respectively, depending on the energy alignment at TRJ.

The calibrated simulation model is used to establish a realistic optimization roadmap of the baseline tandem solar cell. We present four steps to improve the tandem solar cell, considering the same bottom cell. First, we optimize the energy alignment at the TRJ by replacing PEDOT:PSS with NiO$_x$. We calculate an increase in η from 10.63 % to 12.91 % because of the improved energy alignment at TRJ. Second, we calculate an η increase from 12.91 % to 24.37 % by improving the light management. Such an enhancement is achieved by minimizing the current mismatch between the sub-cells and reducing reflectance losses. In this regard, we adjust perovskite thickness from 450 to 312 nm, use 100-nm thick MgF$_2$ as ARC and reduce front metallization from 35 μm (7 %) to 5 μm (1 %). Third, we estimate an efficiency rise from 24.37 % to 25.13 % by improving the transport towards SnO$_2$ in ETL of top cell. Finally, we assess an ultimate efficiency of 26.69 % which is obtained by reducing defect density at perovskite interface with ETL and HTL. It must be noted that further conversion efficiency gains are possible by improving areas of the bottom cell such as the absorber band gap energy and the passivation of the interface CIGS/Mo.

CRediT authorship contribution statement

P. Procel: Writing – original draft, Methodology, Investigation, Conceptualization. **J. Knobbe:** Writing – review & editing, Methodology, Investigation. **N. Rezaei:** Writing – review & editing, Methodology, Investigation, Conceptualization. **V. Zardetto:** Writing – review & editing, Methodology, Investigation. **N. Phung:** Writing – review & editing, Investigation. **M. Ma:** Methodology. **M. Simor:** Methodology. **M. Creatore:** Writing – review & editing, Supervision. **S. Veenstra:** Writing – review & editing, Supervision. **R. Santbergen:** Writing – review & editing, Supervision. **L. Mazzarella:** Writing – review & editing, Methodology. **O. Isabella:** Writing – review & editing, Visualization, Supervision.

Declaration of competing interest

The authors declare that they have no known competing financial interests or personal relationships that could have appeared to influence the work reported in this paper.

Data availability

Data will be made available on request.

Acknowledgement

References

[1] T.J. Jacobsson, A. Hultqvist, S. Svanström, L. Riekehr, U.B. Cappel, E. Unger, H. Rensmo, E.M.J. Johansson, M. Edoff, G. Boschloo, 2-Terminal CIGS-perovskite tandem cells: a layer by layer exploration, Sol. Energy 207 (February) (2020) 270–288.

[2] M. Jošt, T. Bertram, D. Koushik, J.A. Marquez, M.A. Verheijen, M.D. Heinemann, E. Köhnen, A. Al-Ashouri, S. Braunger, F. Lang, B. Rech, T. Unold, M. Creatore, I. Lauermann, C.A. Kaufmann, R. Schlatmann, S. Albrecht, 21.6%-Efficient monolithic perovskite/Cu(in,Ga)Se 2 tandem solar cells with thin conformal hole transport layers for integration on rough bottom cell surfaces, ACS Energy Lett. 4 (2) (Feb. 2019) 583–590.

[3] T. Todorov, T. Gershon, O. Gunawan, Y.S. Lee, C. Sturdevant, L.Y. Chang, S. Guha, Monolithic perovskite-CIGS tandem solar cells via in Situ band gap engineering, Adv. Energy Mater. 5 (23) (2015) 1–6.

[4] Q. Han, Y.T. Hsieh, L. Meng, J.L. Wu, P. Sun, E.P. Yao, S.Y. Chang, S.H. Bae, T. Kato, V. Bermudez, Y. Yang, High-performance perovskite/Cu(In,Ga)Se2 monolithic tandem solar cells, Science 361 (6405) (2018) 904–908.

[5] U. Heske, D. (ZSW) lincot, M. (ZSW) powalla, P. (INL) salome, R. (HZB) schlatman, and A. (EMPA) tiwari, "CIGS white paper,", CIGS Thin-Film Photovoltaics (2019) [Online]. Available: https://cigs-pv.net/wortpresse/wp-content/uploads/2019/04/CIGS_White_Paper_2019_online.pdf.

[6] I. Kafedjiska, G.A. Farias-Basulto, P. Reyes-Figueroa, T. Bertram, A. Al-Ashouri, C. A. Kaufmann, R. Wenisch, S. Albrecht, R. Schlatmann, I. Lauermann, Integration of rough RTP absorbers into CIGS-perovskite monolithic tandems by NiOx(:Cu)+SAM Hole-transporting Bi-layers, Sol. Energy Mater. Sol. Cells 254 (July 2022) (Jun. 2023) 112248.

[7] M. Jošt, E. Köhnen, A. Al-Ashouri, T. Bertram, Š. Tomšič, A. Magomedov, E. Kasparavicius, T. Kodalle, B. Lipovšek, V. Getautis, R. Schlatmann, C. A. Kaufmann, S. Albrecht, M. Topič, Perovskite/CIGS tandem solar cells: from certified 24.2% toward 30% and beyond, ACS Energy Lett. 7 (4) (2022) 1298–1307.

[8] R. Santbergen, R. Mishima, T. Meguro, M. Hino, H. Uzu, J. Blanker, K. Yamamoto, M. Zeman, Minimizing optical losses in monolithic perovskite/c-Si tandem solar cells with a flat top cell, Opt Express 24 (18) (2016) A1288.

[9] M. Jošt, E. Köhnen, A.B. Morales-Vilches, B. Lipovšek, K. Jäger, B. Macco, A. Al-Ashouri, J. Krč, L. Korte, B. Rech, R. Schlatmann, M. Topič, B. Stannowski, S. Albrecht, Textured interfaces in monolithic perovskite/silicon tandem solar cells: advanced light management for improved efficiency and energy yield, Energy Environ. Sci. 11 (12) (2018) 3511–3523.

[10] K. Jäger, L. Korte, B. Rech, S. Albrecht, Numerical optical optimization of monolithic planar perovskite-silicon tandem solar cells with regular and inverted device architectures, Opt Express 25 (12) (2017) A473.

[11] L. Mazzarella, M. Werth, K. Jäger, M. Jošt, L. Korte, S. Albrecht, R. Schlatmann, B. Stannowski, Infrared photocurrent management in monolithic perovskite/silicon heterojunction tandem solar cells by using a nanocrystalline silicon oxide interlayer, Opt Express 26 (10) (2018) A487.

[12] M. Singh, R. Santbergen, I. Syifai, A. Weeber, M. Zeman, O. Isabella, Comparing optical performance of a wide range of perovskite/silicon tandem architectures under real-world conditions, Conf. Rec. IEEE Photovolt. Spec. Conf. 10 (8) (2021) 969–971.

[13] M. Kovačič, J. Krč, K. Savva, S. Maragkaki, E. Stratakis, M. Rashid, M. Tutundzic, Y. Kuang, J. de Wild, T. Aernouts, B. Vermang, M. Topič, Optical simulation study of perovskite/CIGS tandem solar cells with reduced graphene oxide layers, Front. Photonics 3 (May) (2022) 1–12.

[14] L. Mazzarella, Y.H. Lin, S. Kirner, A.B. Morales-Vilches, L. Korte, S. Albrecht, E. Crossland, B. Stannowski, C. Case, H.J. Snaith, R. Schlatmann, Infrared light management using a nanocrystalline silicon oxide interlayer in monolithic perovskite/silicon heterojunction tandem solar cells with efficiency above 25, Adv. Energy Mater. 9 (14) (2019) 1–9.

[15] A. Kumar, S. Singh, M.K.A. Mohammed, A.E. Shalan, Computational modelling of two terminal CIGS/perovskite tandem solar cells with power conversion efficiency of 23.1, Eur. J. Inorg. Chem. 2021 (47) (2021) 4959–4969.

[16] N.E.I. Boukortt, S. Patanè, A.M. AlAmri, D. AlAjmi, K. Bulayyan, N. AlMutairi, Numerical investigation of perovskite and u-CIGS based tandem solar cells using silvaco TCAD simulation, Silicon 15 (1) (Jan. 2023) 293–303.

[17] J. Wang, V. Zardetto, K. Datta, D. Zhang, M.M. Wienk, R.A.J. Janssen, 16.8% Monolithic all-perovskite triple-junction solar cells via a universal two-step solution process, Nat. Commun. 11 (1) (Oct. 2020) 5254.

[18] Synopsys, TCAD Sentaurus: Sentaurus Device User Guide, 2015. *Version K-2015.06*.

[19] R. Santbergen, T. Meguro, T. Suezaki, G. Koizumi, K. Yamamoto, M. Zeman, GenPro4 optical model for solar cell simulation and its application to multijunction solar cells, IEEE J. Photovoltaics 7 (3) (2017) 919–926.

[20] N. Rezaei, P. Procel, M. Simor, Z. Vroon, M. Zeman, O. Isabella, Interdigitated back-contacted structure: A different approach towards high-efficiency ultrathin copper indium gallium (di)selenide solar cells, Prog. Photovoltaics Res. Appl. 28 (9) (Sep. 2020) 899–908.

[21] Z. Ni, C. Bao, Y. Liu, Q. Jiang, W.-Q. Wu, S. Chen, X. Dai, B. Chen, B. Hartweg, Z. Yu, Z. Holman, J. Huang, Resolving spatial and energetic distributions of trap states in metal halide perovskite solar cells, Science 367 (6484) (Mar. 2020) 1352–1358.

[22] R. van Heerden, P. Procel, L. Mazzarella, R. Santbergen, O. Isabella, Slow shallow energy states as the origin of hysteresis in perovskite solar cells, Front. Photonics 3 (4) (May 2022) 401–435.

[23] P. Procel, H. Xu, A. Saez, C. Ruiz-Tobon, L. Mazzarella, Y. Zhao, C. Han, G. Yang, M. Zeman, O. Isabella, The role of heterointerfaces and subgap energy states on transport mechanisms in silicon heterojunction solar cells, Prog. Photovoltaics Res. Appl. 28 (9) (Sep. 2020) 935–945.

[24] E. Aydin, M. De Bastiani, X. Yang, M. Sajjad, F. Aljamaan, Y. Smirnov, M. N. Hedhili, W. Liu, T.G. Allen, L. Xu, E. Van Kerschaver, M. Morales-Masis, U. Schwingenschlögl, S. De Wolf, Zr-Doped indium oxide (IZRO) transparent electrodes for perovskite-based tandem solar cells, Adv. Funct. Mater. 29 (25) (Jun. 2019) 1901741.

[25] Y. Kuang, V. Zardetto, R. van Gils, S. Karwal, D. Koushik, M.A. Verheijen, L. E. Black, C. Weijtens, S. Veenstra, R. Andriessen, W.M.M. Kessels, M. Creatore, Low-temperature plasma-assisted atomic-layer-deposited SnO 2 as an electron transport layer in planar perovskite solar cells, ACS Appl. Mater. Interfaces 10 (36) (Sep. 2018) 30367–30378.

[26] M. Zhang, Q. Chen, R. Xue, Y. Zhan, C. Wang, J. Lai, J. Yang, H. Lin, J. Yao, Y. Li, L. Chen, Y. Li, Reconfiguration of interfacial energy band structure for high-performance inverted structure perovskite solar cells, Nat. Commun. 10 (1) (Dec. 2019) 4593.

[27] R. Pandey, R. Chaujar, Technology computer aided design of 29.5% efficient perovskite/interdigitated back contact silicon heterojunction mechanically stacked tandem solar cell for energy-efficient applications, J. Photon. Energy 7 (2) (2017) 022503.

[28] W. Rehman, D.P. McMeekin, J.B. Patel, R.L. Milot, M.B. Johnston, H.J. Snaith, L. M. Herz, Photovoltaic mixed-cation lead mixed-halide perovskites: links between crystallinity, photo-stability and electronic properties, Energy Environ. Sci. 10 (1) (2017) 361–369.

[29] Q. Zhao, R. Wu, Z. Zhang, J. Xiong, Z. He, B. Fan, Z. Dai, B. Yang, X. Xue, P. Cai, S. Zhan, X. Zhang, J. Zhang, Achieving efficient inverted planar perovskite solar cells with nondoped PTAA as a hole transport layer, Org. Electron. 71 (May) (Aug. 2019) 106–112.

[30] Y. Kim, E.H. Jung, G. Kim, D. Kim, B.J. Kim, J. Seo, Sequentially fluorinated PTAA polymers for enhancing V OC of high-performance perovskite solar cells, Adv. Energy Mater. 8 (29) (Oct. 2018) 1801668.

[31] C. Frisk, C. Platzer-Björkman, J. Olsson, P. Szaniawski, J.T. Wätjen, V. Fjällström, P. Salomé, M. Edoff, Optimizing Ga-profiles for highly efficient Cu(In, Ga)Se 2 thin film solar cells in simple and complex defect models, J. Phys. D Appl. Phys. 47 (48) (Dec. 2014) 485104.

[32] R. Kotipalli, O. Poncelet, G. Li, Y. Zeng, L.A. Francis, B. Vermang, D. Flandre, Addressing the impact of rear surface passivation mechanisms on ultra-thin Cu(In, Ga)Se2 solar cell performances using SCAPS 1-D model, Sol. Energy 157 (December 2016) (Nov. 2017) 603–613.

[33] T.M. Friedlmeier, P. Jackson, A. Bauer, D. Hariskos, O. Kiowski, R. Wuerz, M. Powalla, Improved photocurrent in Cu(in,Ga)Se 2 solar cells: from 20.8% to 21.7% efficiency with CdS buffer and 21.0% Cd-free, IEEE J. Photovoltaics 5 (5) (Sep. 2015) 1487–1491.

[34] T. Hara, T. Maekawa, S. Minoura, Y. Sago, S. Niki, H. Fujiwara, Quantitative assessment of optical gain and loss in submicron-textured CuIn1−xGaxSe2 solar cells fabricated by three-stage coevaporation, Phys. Rev. Appl. 2 (3) (Sep. 2014) 034012.

[35] H. Tang, Y. Shang, W. Zhou, Z. Peng, Z. Ning, Energy level tuning of PEDOT:PSS for high performance tin-lead mixed perovskite solar cells, Sol. RRL 3 (2) (Feb. 2019) 1800256.

[36] A.J. Olivares, I. Cosme, M.E. Sanchez-Vergara, S. Mansurova, J.C. Carrillo, H. E. Martinez, A. Itzmoyotl, Nanostructural modification of PEDOT:PSS for high

[37] A.M. Nardes, On the Conductivity of PEDOT:PSS Thin Films, vol. 41, 2007. 2007.

[38] D. Koushik, M. Jošt, A. Dučinskas, C. Burgess, V. Zardetto, C. Weijtens, M. A. Verheijen, W.M.M. Kessels, S. Albrecht, M. Creatore, Plasma-assisted atomic layer deposition of nickel oxide as hole transport layer for hybrid perovskite solar cells, J. Mater. Chem. C 7 (40) (2019) 12532–12543.

[39] M.T. Greiner, M.G. Helander, W.-M. Tang, Z.-B. Wang, J. Qiu, Z.-H. Lu, Universal energy-level alignment of molecules on metal oxides, Nat. Mater. 11 (1) (2011) 76–81.

[40] N. Rezaei, O. Isabella, Z. Vroon, M. Zeman, Quenching Mo optical losses in CIGS solar cells by a point contacted dual-layer dielectric spacer: a 3-D optical study, Opt Express 26 (2) (Jan. 2018) A39.

[41] N. Rezaei, Opto-electrical Modelling of CIGS Solar Cells, TU Delft, 2020.

[42] T. de Vrijer, D. van Nijen, H. Parasramka, P.A. Procel Moya, Y. Zhao, O. Isabella, A. H.M. Smets, The fundamental operation mechanisms ofnc-SiO>0:H based tunnel recombination junctions revealed, Sol. Energy Mater. Sol. Cells 236 (August 2021) (Mar. 2022) 111501.

[43] M. De Bastiani, A.S. Subbiah, E. Aydin, F.H. Isikgor, T.G. Allen, S. De Wolf, Recombination junctions for efficient monolithic perovskite-based tandem solar cells: physical principles, properties, processing and prospects, Mater. Horiz. 7 (11) (2020) 2791–2809.

[44] D.H. Kim, C.P. Muzzillo, J. Tong, A.F. Palmstrom, B.W. Larson, C. Choi, S. P. Harvey, S. Glynn, J.B. Whitaker, F. Zhang, Z. Li, H. Lu, M.F.A.M. van Hest, J. J. Berry, L.M. Mansfield, Y. Huang, Y. Yan, K. Zhu, Bimolecular additives improve wide-band-gap perovskites for efficient tandem solar cells with CIGS, Joule 3 (7) (2019) 1734–1745.

[45] N. Rezaei, O. Isabella, P. Procel, Z. Vroon, M. Zeman, Optical study of back-contacted CIGS solar cells, Opt Express 27 (8) (2019) A269.

[46] J.H. Won, H. Choi, S.H. Han, B.K. Park, T.-M. Chung, J.H. Han, Polycrystalline and high purity SnO2 films by plasma-enhanced atomic layer deposition using H2O plasma at very low temperatures of 60–90 °C, Vacuum 196 (November 2021) (Feb. 2022) 110739.

[47] C. Zhang, H. Wang, H. Li, Q. Zhuang, C. Gong, X. Hu, W. Cai, S. Zhao, J. Chen, Z. Zang, Simultaneous passivation of bulk and interface defects through synergistic effect of anion and cation toward efficient and stable planar perovskite solar cells, J. Energy Chem. 63 (2021) 452–460.

[48] H. Zhang, F. Ye, W. Li, J. Yao, R.S. Gurney, D. Liu, C. Xiong, T. Wang, Bright perovskite light-emitting diodes with improved film morphology and reduced trap density via surface passivation using quaternary ammonium salts, Org. Electron. 67 (November 2018) (2019) 187–193.

[49] W. Shen, Y. Dong, F. Huang, Y.-B. Cheng, J. Zhong, Interface passivation engineering for hybrid perovskite solar cells, Mater. Reports Energy 1 (4) (2021) 100060.

[50] J. Kim, A. Ho-Baillie, S. Huang, Review of novel passivation techniques for efficient and stable perovskite solar cells, Sol. RRL 3 (4) (Apr. 2019) 1–16.

[51] M. Nakamura, K. Yamaguchi, Y. Kimoto, Y. Yasaki, T. Kato, H. Sugimoto, Cd-free Cu(in,Ga)(Se,S) 2 thin-film solar cell with record efficiency of 23.35, IEEE J. Photovoltaics 9 (6) (Nov. 2019) 1863–1867.

[52] J. de Wild, G. Birant, G. Brammertz, M. Meuris, J. Poortmans, B. Vermang, Ultrathin Cu(in,Ga)Se2 solar cells with Ag/AlOx passivating back reflector, Energies 14 (14) (Jul. 2021) 4268.

[53] G. Birant, J. Mafalda, R. Scaffidi, J. de Wild, D.G. Buldu, T. Kohl, G. Brammertz, M. Meuris, J. Poortmans, B. Vermang, Rear surface passivation of ultra-thin CIGS solar cells using atomic layer deposited HfO x, EPJ Photovoltaics 11 (10) (Dec. 2020).